Statistical Characteristics of the Large-Scale Response of Coastal Sea Level to Atmospheric Forcing

J. S. ALLEN AND D. W. DENBO

College of Oceanography, Oregon State University, Corvallis, OR 97331

(Manuscript received 18 November 1983, in final form 5 April 1984)

ABSTRACT

As part of a study of the large-scale response of coastal sea level to atmospheric forcing along the west coast of North America during June–September 1973, Halliwell and Allen calculate space- and time-lagged cross-correlation coefficients $R_{\tau\zeta}$ between adjusted sea level ζ at fixed alongshore locations $\zeta(y_0)$ and the alongshore component of the wind stress τ at general alongshore positions $\tau(y)$. Similarly, correlation coefficients $R_{\zeta\zeta}$ and $R_{\tau\tau}$ involving, respectively, $\zeta(y_0)$ versus $\zeta(y)$ and $\tau(y_0)$ versus $\tau(y)$ are computed. The $R_{\tau\zeta}$ correlations show a consistent asymmetry in time and space lag (t_L, y_L), with maximum values of $R_{\tau\zeta}$ found for $\tau(y)$ to the south of $\zeta(y_0)$ and leading in time. The $R_{\tau\tau}$ correlations are typically symmetric in t_L and in y_L, while $R_{\zeta\zeta}$ generally show sea level fluctuations to the south leading those to the north in time. It is shown here that the observed correlation coefficients involving ζ are consistent with those derived from solutions to the forced, first-order wave equation with a linear friction term where an assumed form of $R_{\tau\tau}$, based on observations, is used as a forcing function. Similar investigations are carried out in the frequency domain where corresponding theoretical space-lagged squared coherences and phases are calculated. Qualitative agreement with observed behavior is obtained in several instances for the space-lagged statistical functions in both time and frequency domains. Additional new results include theoretical expressions for the relation in wind-forced regions of alongshore propagation velocities of ζ, determined from lagged cross-correlation coefficients or cross-spectral phase differences between variables at different alongshore positions, to the free-wave propagation speed c, the determination of c from $R_{\tau\zeta}$, the variation with frequency of alongshore coherence scales of ζ and of coherence and phase between ζ and local τ.

1. Introduction

The behavior of large-scale fluctuations in coastal sea level along the west coast of North America during summer 1973 has been studied by Halliwell and Allen (1984, hereafter referred to as HA). In this context, large scale means alongshore spatial scales L_y that are larger than the width L_x of the continental shelf and slope, i.e., $L_y \gg L_x \approx 100$ km. In particular, HA investigated the response of coastal sea level to large-scale atmospheric forcing, represented by the alongshore component of the wind stress at the coast. Among other results, it was found that a single, forced, first-order wave equation with a linear friction term was capable of reasonably modeling the response of observed sea-level fluctuations along the Oregon and Washington coast to observed winds.

The forced, first-order wave equation was derived originally by Gill and co-workers (Gill and Schumann, 1974; Gill and Clarke, 1974). For example, Gill and Schumann (1974) showed it to be the governing equation for the alongshore and time-dependent behavior of each cross-shelf mode in a model of forced, barotropic shelf waves in the long wave ($L_y \gg L_x$), nondispersive limit. The same equation has been shown to apply under the long-wave approximation in the case of a continuously stratified ocean (Clarke, 1977) if the variables are expanded in terms of generalized cross-shelf modes dependent on both the cross-shelf and vertical coordinates.

With y the alongshore coordinate, positive northward for the Pacific coast, t the time variable, and $Y(y, t)$ the amplitude of the lowest cross-shelf mode, the forced, first-order wave equation with a linear friction term is

$$c^{-1}Y_t + Y_y + (cT_F)^{-1}Y = b\tau(y, t), \qquad (1.1)$$

where subscripts (t, y) denote partial differentiation, c is the lowest-mode nondispersive free-wave speed, T_F a frictional decay time, b a constant dependent on topography and stratification, and $\tau(y, t)$ is the alongshore component of the wind stress at the coast. The application of a single wave equation (1.1) to model-adjusted coastal sea level $\zeta(y, t)$ observations involves the assumption that the amplitude of the lowest cross-shelf mode dominates the fluctuations of sea level at the coast and thus that $\zeta \propto Y$. Moreover, under the long-wave approximation, the alongshore velocity v is assumed to be in geostrophic balance so that fluctuations in $v \propto \zeta \propto Y$. These assumptions are supported by observations off Oregon (Smith, 1974; Kundu and Allen, 1976; Huyer *et al.*, 1978; see also HA).

The linear friction term in (1.1) was added in an *ad hoc* manner by Gill and Schumann (1974) as the

simplest, reasonable method to represent dissipative effects. This term follows from the presence of linear bottom friction in both barotropic and stratified cases for frequencies ω such that $\omega T_F \gg 1$ (Brink and Allen, 1978, 1983; Brink, 1982; Allen, 1984). Although the simple addition of a linear term $(cT_F)^{-1}Y$ in (1.1) is not a strictly valid representation of bottom friction effects for all conditions, it is utilized in HA and here in the original spirit of Gill and Schumann (1974).

A finding of particular interest in HA concerns the patterns of space- and time-lagged cross-correlation coefficients between adjusted sea level or wind stress at one location, $\zeta(y_0)$, $\tau(y_0)$, and sea level or wind stress at general alongshore positions $\zeta(y)$, $\tau(y)$. The essential features of those results are summarized in Fig. 1 in the form of space- and time-lagged cross-correlation coefficients calculated from the same data using space-averaged covariances, as described in Appendix A. In particular, correlation coefficients of space-averaged $\zeta(y_0)$ versus $\zeta(y)[\hat{R}_{\zeta\zeta}]$, $\tau(y_0)$ versus $\tau(y)[\hat{R}_{\tau\tau}]$, and $\zeta(y_0)$ versus $\tau(y)[\hat{R}_{\tau\zeta}]$, for two domains, north and south, are shown in Fig. 1.

The $\hat{R}_{\zeta\zeta}$ correlations in both domains show a definite tilt to the contours, indicating fluctuations to the south lead those to the north. The smaller slope in the southern region of a line through the maximum correlation at each space lag seems to indicate lower propagation velocities there than in the north. Also, there is a noticeably longer time scale for the southern ζ fluctuations. The $\hat{R}_{\tau\tau}$ correlations are much more symmetric in time lag and space lag than those found for $\hat{R}_{\zeta\zeta}$, with similar time and space scales in both regions. The $\hat{R}_{\tau\zeta}$ correlations in both domains have maximum values for τ fluctuations at locations south of, and leading in time, the fluctuations in ζ. For the northern domain, the space and time lags for maximum correlation between $\zeta(y_0)$ and $\tau(y)$ are about 540 km and 1.75 days, while for the southern domain the corresponding lags are about 200 km and 1 day. Qualitatively similar patterns were found in the $R_{\tau\zeta}$ correlations for all the individual sea level stations examined in HA. Related space-lagged frequency domain calculations in HA of squared coherences between $\zeta(y_0)$ and $\tau(y)$ also show asymmetries in space lag, generally similar to $R_{\tau\zeta}$ at low frequencies (<0.2 cpd), but with a change in structure at higher frequencies.

The observation from $R_{\tau\zeta}$ in HA, that, in a strongly wind-forced region, τ from locations south of the position of the ζ measurement is generally more highly correlated with ζ than τ from the same location as ζ (local τ), is striking and, although this structure of $R_{\tau\zeta}$ is a simple observational result, it is evidently new. In the past, evidence for wind driving of shelf currents frequently has been derived from the correlation of local τ and the alongshore current v or of local τ and ζ. This method has been utilized because, for time periods greater than one day, the variability in v (and hence in ζ) is generally the strongest signal in the shelf velocity field and τ is typically only measured locally. Also, v and ζ often have significant correlations with local τ. [Notable exceptions to this procedure (Hamon, 1976; Clarke, 1977; HA) have involved the use of τ

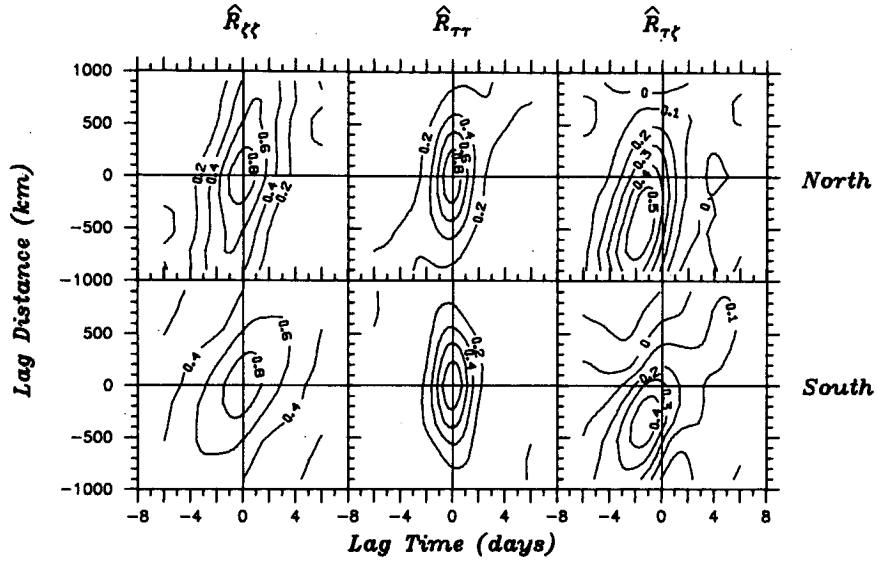

FIG. 1. Observed space- and time-lagged cross-correlation coefficients calculated from space-averaged covariances for adjusted coastal sea level ζ and the alongshore component of the wind stress τ, $\hat{R}_{\zeta\zeta}[\zeta(y_0)$ vs $\zeta(y)]$, $\hat{R}_{\tau\tau}[\tau(y_0)$ vs $\tau(y)]$, and $\hat{R}_{\tau\zeta}[\zeta(y_0)$ vs $\tau(y)]$, with the gridded data analyzed by Halliwell and Allen (1984) from along the west coast of North America during June–September 1973 (see Appendix A). Correlation coefficients in the top panel involve data only from a northern domain (41.8 to 52.2°N) and in the bottom panel from a southern domain (33 to 41.8°N). The contour intervals are 0.2 for $\hat{R}_{\zeta\zeta}$ and $\hat{R}_{\tau\tau}$ and 0.1 for $\hat{R}_{\tau\zeta}$.

integrated alongshore in the appropriate direction to test solutions of (1.1).] An examination of (1.1), or of the depth-integrated momentum equation (e.g., see Allen and Smith, 1981) shows, however, that, unless the shelf flow field is totally dominated by friction, there is no reason for a perfect correlation of local τ and ζ or v. Rather, (1.1) implies that local τ should be correlated with a particular combination of ζ and of the time and space derivatives, ζ_t and ζ_y. Thus, it is not surprising that ζ may have a higher correlation with τ at some other alongshore position. That position, in fact, can be determined from the solution to (1.1). One purpose of this paper is to show that the $R_{\tau\zeta}$ correlations found from observations in HA are consistent with those derived from solutions to the forced, first-order wave equation (1.1).

Space-lagged cross-correlation coefficients and cross-spectra are natural statistical functions to examine in observational studies of alongshore variations in shelf flow fields. Although the observed patterns in space-lag and time-lag (or frequency) of these quantities show very definite structure, there is at present no direct way of understanding how that structure relates to physical models. This lack of identification of statistical functions with even qualitative theoretical predictions applies not only to the new results in HA, but also to quantities commonly calculated in wind-forced regions such as alongshore propagation speeds for fluctuations in ζ or v from lagged cross-correlation coefficients or from cross-spectral phase differences between variables measured at different alongshore positions, alongshore coherence scales of ζ or v as a function of frequency, and coherence and phase between v and local τ. To help remedy this shortcoming, we present here a theoretical study of statistical characteristics of solutions to the first-order wave equation (1.1). We utilize (1.1) based on the strong support found in HA for its applicability to the northwest Pacific coast. The procedure is to obtain representative results in idealized cases, with parameters varied one at a time. The basic objective is to translate theoretical model output into the same language used in discussing observations and thus to build insight into the nature of theoretical predictions for relevant statistical variables and the dependence of these predictions on different physical effects.

2. Analysis—Time domain

Defining the variable

$$y' = y/c, \tag{2.1}$$

and then dropping the prime (i.e., $y' \rightarrow y$), we write (1.1) in the form

$$Y_t + Y_y + (T_F)^{-1}Y = cb\tau(y, t). \tag{2.2}$$

Note that now both y and t have dimensions of time and that the characteristics of (2.2) have slope $dy/dt = 1$. The solution to (2.2), appropriate here where τ is assumed specified for all y and t, is

$$Y(y, t) = cb \int_0^\infty \exp(-r/T_F)\, \tau(y - r, t - r)dr. \tag{2.3}$$

The solution (2.3) for Y may be utilized to find expressions for the resulting space- and time-lagged cross-correlation coefficients described for ζ and τ in Section 1. In particular, we assume that $\tau(y, t)$ is a stationary random function of time with zero mean and with variance $\langle\tau^2(y)\rangle$, where the angle brackets here denote the time average

$$\langle\phi\rangle = \lim_{T_0\rightarrow\infty} \frac{1}{2T_0} \int_{-T_0}^{T_0} \phi(t)dt. \tag{2.4}$$

We define

$$y_1 = y + y_L, \quad t_1 = t + t_L, \tag{2.5a,b}$$

where y_L and t_L are space and time lags, respectively, and use the shorthand notation

$$\left.\begin{aligned} Y(y, t) &= Y, \quad \tau(y, t) = \tau, \\ Y(y_1, t_1) &= Y_1, \quad \tau(y_1, t_1) = \tau_1 \end{aligned}\right\}. \tag{2.6}$$

The wind stress is assumed to be characterized by a space- and time-lagged cross-correlation coefficient, that is a function of $y_L = y_1 - y$ and $t_L = t_1 - t$ of the form

$$\frac{\langle\tau_1\tau\rangle}{\langle\tau_1^2\rangle^{1/2}\langle\tau^2\rangle^{1/2}} = R_{\tau\tau}(y_L, t_L)$$

$$= \exp[-(y_L^2\chi^2 + 2\lambda\chi y_L t_L + t_L^2)T^{-2}], \tag{2.7a}$$

where

$$\chi = cT/L. \tag{2.7b}$$

Here T and L are time and space exponential decay scales for $R_{\tau\tau}$ [recall the scaling (2.1)] and $\lambda(|\lambda| \leqslant 1)$ is a parameter that governs rotation in the (t_L, y_L) plane of the decay ellipse,

$$T^2 = y_L^2\chi^2 + 2\lambda\chi y_L t_L + t_L^2, \tag{2.8}$$

in the argument of the exponential in (2.7a). Such a rotation would correspond to a preferred direction of propagation for fluctuations in τ. Note that with assumption (2.7), the variance of τ may still be a function of y, $\langle\tau^2\rangle = \langle\tau^2(y)\rangle$, in which case the cross-covariance

$$\langle\tau_1\tau\rangle = \langle\tau^2(y_1)\rangle^{1/2}\langle\tau^2(y)\rangle^{1/2}R_{\tau\tau}(y_L, t_L), \tag{2.9}$$

depends on y, as well as on y_L and t_L. The assumed form (2.7) of $R_{\tau\tau}$ is compared with observed $\hat{R}_{\tau\tau}$ from Fig. 1 in Section 4.

It is useful to obtain $\langle Y_1 Y\rangle$ from the solution to

$$\langle Y_1 Y\rangle_y + 2T_F^{-1}\langle Y_1 Y\rangle = cb(\langle\tau_1 Y\rangle + \langle\tau Y_1\rangle), \tag{2.10}$$

which may be readily derived from (2.2).

To obtain $\langle\tau_1 Y\rangle$, we multiply (2.3) by τ_1 and average, which gives

$$\langle \tau_1 Y \rangle = cb \int_0^\infty \exp(-r/T_F) \times \langle \tau(y_1, t_1)\tau(y - r, t - r)\rangle dr. \quad (2.11)$$

With (2.7), (2.11) is

$$\langle \tau_1 Y \rangle = cb \int_0^\infty \exp(-r/T_F)\langle \tau^2(y_1)\rangle^{1/2}\langle \tau^2(y - r)\rangle^{1/2} \times R_{\tau\tau}(y_L + r, t_L + r)dr. \quad (2.12)$$

Thus, as a result of the fact that Y is determined in (2.3) by an integral over τ, $\langle \tau_1 Y \rangle$ is determined in (2.11) by an integral over $\langle \tau_1 \tau \rangle$. In a similar manner, we obtain

$$\langle \tau Y_1 \rangle = cb \int_0^\infty \exp(-r/T_F)\langle \tau^2(y)\rangle^{1/2}\langle \tau^2(y_1 - r)\rangle^{1/2} \times R_{\tau\tau}(r - y_L, r - t_L)dr. \quad (2.13)$$

The solution to (2.10) gives $\langle Y_1 Y \rangle$ directly in a convenient form. We note that $\langle Y_1 Y \rangle$ may also be found, of course, by averaging the product $Y_1 Y$ using (2.3). Identical results are obtained after some algebraic manipulation of the latter expression.

a. $\langle \tau^2 \rangle_y = 0$

We first consider the case of uniform τ-variance,

$$\langle \tau^2 \rangle = \tau_0^2 = \text{constant}. \quad (2.14)$$

As a result, $\langle Y_1 Y \rangle_y = 0$ and the solution to (2.10) is

$$\langle Y_1 Y \rangle = \frac{1}{2} T_F cb(\langle \tau_1 Y \rangle + \langle \tau Y_1 \rangle). \quad (2.15)$$

For $y_L = 0$, (2.15) gives the variance of Y as

$$\langle Y^2 \rangle = T_F cb \langle \tau Y \rangle. \quad (2.16)$$

With (2.14) and the assumed form (2.7) for $\langle \tau_1 \tau \rangle$, the integrals in (2.12) and (2.13) may be evaluated explicitly to give analytical expressions for

$$R_{YY} = \frac{\langle Y_1 Y \rangle}{\langle Y_1^2 \rangle^{1/2}\langle Y^2 \rangle^{1/2}}, \quad (2.17)$$

$$R_{\tau Y} = \frac{\langle \tau_1 Y \rangle}{\langle \tau_1^2 \rangle^{1/2}\langle Y^2 \rangle^{1/2}}. \quad (2.18)$$

These are written out in Appendix B. Note that with (2.14),

$$\langle Y_1^2 \rangle^{1/2} = \langle Y^2 \rangle^{1/2}, \quad \langle \tau_1^2 \rangle^{1/2} = \tau_0,$$
$$R_{YY} = R_{YY}(y_L, t_L), \qquad R_{\tau Y} = R_{\tau Y}(y_L, t_L).$$

b. $\langle \tau^2 \rangle_y \neq 0$

To investigate effects of y-dependence on the variance of τ, we choose a specific, idealized case and assume that

$$\langle \tau^2(y) \rangle = \tau_0^2 \exp(-2y^2\delta^2), \quad (2.19)$$

where $\delta = c/D$ and D is an exponential spatial decay scale about $y = 0$ for the standard deviation $\langle \tau^2 \rangle^{1/2}$.

Again, $\langle Y_1 Y \rangle$ may be obtained from the solution to (2.10), which here is

$$\langle Y_1 Y \rangle = cb \int_0^\infty \exp(-2r/T_F) \times [\langle \tau_1 Y(y - r)\rangle + \langle \tau Y_1(y - r)\rangle]dr. \quad (2.20)$$

Using (2.19), we can calculate $\langle \tau_1 Y \rangle$ and $\langle \tau \bar{Y}_1 \rangle$ from (2.12) and (2.13) and $\langle Y_1 Y \rangle$ from (2.20). The resulting expressions for $R_{YY} = R_{YY}(y_L, t_L; y)$, $R_{\tau Y} = R_{\tau Y}(y_L, t_L; y)$, and $\langle Y^2(y) \rangle$ are given in Appendix B.

3. Analysis—Frequency domain

Although frequency domain results may be obtained from Fourier transforms of $\langle Y_1 Y \rangle$ and $\langle \tau_1 Y \rangle$, as is done later with $\langle \tau_1 \tau \rangle$, we find it more useful for interpretation to work directly with the Fourier transform of (2.2). Consequently, we regard $\tau(y, t)$ as a sample function of an ergodic, stationary random process. We assume initially that the values of all variables outside a finite interval $-T_0 \leq t \leq T_0$ are replaced with zero and utilize the Fourier transform

$$\bar{Y}(y, \omega) = \int_{-\infty}^{+\infty} Y(y, t)e^{i\omega t}dt. \quad (3.1)$$

Spectra and cross-spectra are obtained from an ensemble average of the appropriate product followed by division by $2T_0$ and the limit $T_0 \to \infty$. That combined operation is denoted by braces as in (3.4).

The Fourier transform of (2.2) gives

$$\bar{Y}_y + (T_F^{-1} - i\omega)\bar{Y} = cb\bar{\tau}, \quad (3.2)$$

with solution

$$\bar{Y}(y, \omega) = cb \int_0^\infty \exp[-(T_F^{-1} - i\omega)s]\bar{\tau}(y - s, \omega)ds. \quad (3.3)$$

A shorthand notation similar to (2.6) is employed, e.g., $\bar{Y}(y, \omega) = \bar{Y}$, $\bar{Y}(y_1, \omega) = \bar{Y}_1$, where $y_1 = y + y_L$ as in (2.5a). An asterisk is used to denote complex conjugate, e.g., Y^*. The following analysis parallels that in Section 2.

We assume that the wind stress is characterized by space-lagged cross-spectra of the form

$$\frac{\{\bar{\tau}\bar{\tau}^*\}}{\{\bar{\tau}\bar{\tau}^*\}^{1/2}\{\bar{\tau}_1\bar{\tau}_1^*\}^{1/2}} = S_{\tau\tau}(y_L, \omega), \quad (3.4)$$

where, corresponding to the Fourier transform with respect to t_L of $\langle \tau_1 \tau \rangle$ in (2.9),

$$S_{\tau\tau}(y_L, \omega) = \exp(-dy_L^2 - ey_L), \quad (3.5a)$$

$$d = (c^2/L^2)(1 - \lambda^2), \quad e = i\omega\lambda\chi, \quad (3.5b,c)$$

$$\{\bar{\tau}\bar{\tau}^*(y)\} = \langle\tau^2(y)\rangle P(\omega), \quad (3.6a)$$

$$P(\omega) = T\pi^{1/2}\exp(-\tfrac{1}{4}\omega^2T^2). \quad (3.6b)$$

The following analysis and results are *not* dependent on the particular form of $P(\omega)$ in (3.6b).

It is convenient to find $\{\bar{Y}\bar{Y}^*\}$ from the solution to

$$\{\bar{Y}\bar{Y}^*\}_y + 2T_F^{-1}\{\bar{Y}\bar{Y}^*\} = cb(\{\bar{Y}\bar{\tau}^*\} + \{\bar{\tau}\bar{Y}^*\}), \quad (3.7)$$

which may be derived from (3.2).

To obtain $\{\bar{Y}\bar{\tau}^*\}$, we multiply (3.3) by $\bar{\tau}^*$ and average, which gives

$$\{\bar{Y}\bar{\tau}^*\} = cb\int_0^\infty \exp[-(T_F^{-1} - i\omega)s]$$

$$\times \{\bar{\tau}\bar{\tau}^*(y-s)\}^{1/2}\{\bar{\tau}\bar{\tau}^*(y_1)\}^{1/2}S_{\tau\tau}(-y_L - s)ds. \quad (3.8)$$

Similarly, we obtain

$$\{\bar{\tau}\bar{Y}^*\} = cb\int_0^\infty \exp[-(T_F^{-1} + i\omega)s]$$

$$\times \{\bar{\tau}\bar{\tau}^*(y)\}^{1/2}\{\bar{\tau}\bar{\tau}^*(y_1 - s)\}^{1/2}S_{\tau\tau}(s - y_L)ds. \quad (3.9)$$

a. $\langle\tau^2\rangle_y = 0$

For the case of uniform τ-variance (2.14), $\{\bar{\tau}\bar{\tau}^*\} = \tau_0^2P(\omega)$, $\{\bar{Y}\bar{Y}^*\}_y = 0$, and it follows from (3.7) that

$$\{\bar{Y}\bar{Y}^*\} = \tfrac{1}{2}T_Fcb(\{\bar{Y}\bar{\tau}^*\} + \{\bar{\tau}\bar{Y}^*\}). \quad (3.10)$$

The integrals in (3.8) and (3.9) may be evaluated to give analytical expressions for the space-lagged cross-spectral quantities

$$S_{YY} = \frac{\{\bar{Y}\bar{Y}^*\}}{\{\bar{Y}\bar{Y}^*\}^{1/2}\{\bar{Y}_1\bar{Y}^*\}^{1/2}}, \quad (3.11)$$

$$S_{\tau Y} = \frac{\{\bar{Y}\bar{\tau}^*\}}{\{\bar{Y}\bar{Y}^*\}^{1/2}\{\bar{\tau}_1\bar{\tau}^*\}^{1/2}}. \quad (3.12)$$

These are written out in Appendix C, where, with (2.14), $S_{YY} = S_{YY}(y_L, \omega)$ and $S_{\tau Y} = S_{\tau Y}(y_L, \omega)$.

b. $\langle\tau^2\rangle_y \neq 0$

We assume again that $\langle\tau^2(y)\rangle$ is given by (2.19). In this case, the solution of (3.7) gives

$$\{\bar{Y}\bar{Y}^*\} = cb\int_0^\infty \exp(-2T_F^{-1}s)[\{\bar{Y}\bar{\tau}^*(y-s)\}$$

$$+ \{\bar{\tau}\bar{Y}^*(y-s)\}]ds. \quad (3.13)$$

Using (2.19) in (3.6), we can calculate $\{\bar{Y}\bar{\tau}^*\}$, and $\{\bar{\tau}\bar{Y}^*\}$ from (3.8) and (3.9) and $\{\bar{Y}\bar{Y}^*\}$ from (3.13). The resulting expressions for $S_{YY} = S_{YY}(y_L, \omega; y)$ and $S_{\tau Y} = S_{\tau Y}(y_L, \omega; y)$ are given in Appendix C.

In Section 5, the space-lagged cross-spectra are presented in terms of the coherence squared C and the phase Θ where, e.g.,

$$C_{\tau Y} = |S_{\tau Y}|^2, \quad \Theta_{\tau Y} = \tan^{-1}[\mathrm{Im}(S_{\tau Y})/\mathrm{Re}(S_{\tau Y})], \quad (3.14a,b)$$

and where Re and Im denote real and imaginary parts.

4. Results—Time domain

a. $\langle\tau^2\rangle_y = 0$

We utilize the assumed form of $R_{\tau\tau}$ in (2.7) and calculate R_{YY} and $R_{\tau Y}$ for various combinations of the parameters c, T_F, L, T, and λ in the case of uniform τ-variance (2.14). Based on the observed $R_{\tau\tau}$-correlation patterns in Fig. 1, we choose for a basic set of parameters the values

$$L = 500 \text{ km}, \quad T = 1.5 \text{ days}, \quad \lambda = 0. \quad (4.1a)$$

Also, based on observed $\hat{R}_{\zeta\zeta}$ and $\hat{R}_{\tau\zeta}$ from the northern domain and results to follow we choose

$$c = 300 \text{ km day}^{-1}, \quad T_F = 3 \text{ days}. \quad (4.1b)$$

To gain an understanding of how differences in the parameters of the problem affect the statistics of the solution, we vary individually T_F, L, and λ, where the variations of T_F and L correspond to changes in the dimensionless parameters T_F/T and $\chi = cT/L$, respectively. Except where noted, the parameter values used in the following calculations correspond to those in (4.1). The positive y-direction will be referred to as northward, as appropriate for the Pacific coast of North America.

The $R_{\tau\tau}$ for the basic case (4.1a) is plotted in Fig. 2. We emphasize that $R_{\tau\tau}$ in (2.7) is chosen for analytical convenience as a qualitative representation only of observed values. In Fig. 3, the assumed $R_{\tau\tau}$, with parameters (4.1a), is compared for $y_L = 0$ and $t_L = 0$ with the observed $\hat{R}_{\tau\tau}$ in Fig. 1. The correspondence is reasonable, with the assumed values decaying more rapidly than the observed for increasing t_L and y_L, as might be expected for (2.7).

Also shown in Fig. 2 are $R_{\tau\tau}$ for $\lambda = \pm 0.5$. These values of λ were chosen, with L and T the same as in (4.1), to represent the situation where τ-fluctuations have a dominant tendency to propagate either northward ($\lambda = -0.5$) or southward ($\lambda = +0.5$). The magnitude of the propagation velocity of τ-fluctuations for both of these values of λ is 667 km day^{-1}. Note that both t_L and y_L are measured in days; y_L may be converted to km by multiplying by $c = 300$ km day^{-1}.

The expression for the variance of Y in (B4) shows that the nondimensionalized variance $\langle Y^2\rangle_N = \langle Y^2\rangle/(cb\tau_0T)^2$ depends on the parameters T, $\beta_0 = (1/2)T_F^{-1}$, and $\alpha = T^{-2}(\chi^2 + 2\lambda\chi + 1)$ and that $\langle Y^2\rangle_N \sim T_F(1/2)(\pi/\alpha)^{1/2}T^{-2}$ for $T_F^{-1} \to 0$. Thus, as friction goes to zero, the variance $\langle Y^2\rangle_N$ is unbounded, resulting from the resonant forcing of (2.2) at alongshore wavenumbers $l = \omega$. For fixed T_F/T, the magnitude of $\langle Y^2\rangle_N$ depends only on αT^2, increasing as αT^2 decreases.

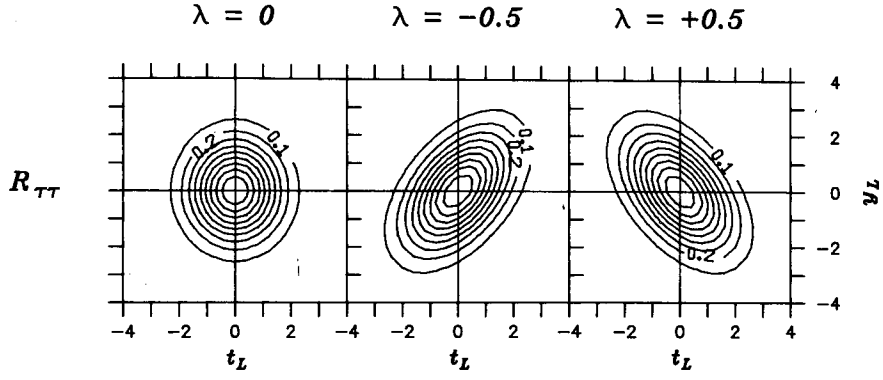

FIG. 2. Assumed form (2.7) for $R_{\tau\tau}(t_L, y_L)$ with parameters (4.1a) for $\lambda = 0$, -0.5, and $+0.5$. Contour interval 0.1.

Note that $\alpha^{-1/2}$ is a decay time for $R_{\tau\tau}$ in the (t_L, y_L)-plane along the characteristic line $y_L = t_L$. Consequently, for fixed T_F, whatever the individual values of c, T, L and λ are, $T^2\langle Y^2\rangle_N$ depends only on the decay time $\alpha^{-1/2}$ of $R_{\tau\tau}$ along $y_L = t_L$ and it increases as $\alpha^{-1/2}$ increases.

Plots of R_{YY} and $R_{\tau Y}$ for $T_F = 1$, 3, 6 days are shown in Fig. 4. The maximum values, R_{YYm} and $R_{\tau Ym}$, of R_{YY} and $R_{\tau Y}$ for each space lag y_L and the corresponding values of t_L at which the maximum occurs (t_{Lm}, y_{Lm}) are plotted in Fig. 5.

The R_{YY} contour lines possess the symmetry $R_{YY}(t_L, y_L) = R_{YY}(-t_L, -y_L)$ as would be expected in the case $\langle\tau^2\rangle_y = 0$ and $\langle Y^2\rangle_y = 0$. The contours of R_{YY} are tilted, corresponding to southern stations (more negative y_L) leading northern stations, in the same sense as found in the observations (Fig. 1). The spatial correlation scale from R_{YY}, defined approximately as $|y_{Lm}|$ for $R_{YY} = 0.7$, increases as T_F increases (Fig. 5). For $T_F = 3$ and 6 days, it is much larger than the correlation scale of τ from $R_{\tau\tau}$, in agreement with observations (Fig. 1). The values of (t_{Lm}, y_{Lm}) for R_{YYm} (Fig. 5) show that characteristic dimensionless velocities c_m of the forced Y-fluctuations, determined using these lags $(c_m = y_{Lm}/t_{Lm})$, vary with y_{Lm} and T_F such that they

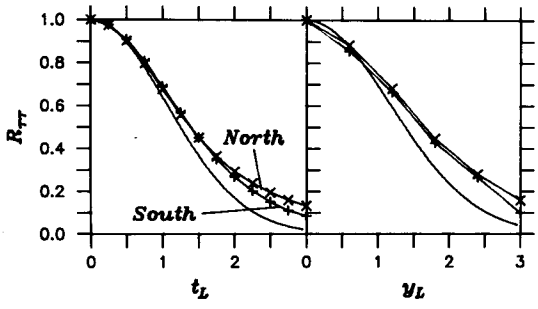

FIG. 3. Comparison for $y_L = 0$ and $t_L = 0$ of assumed $R_{\tau\tau}(t_L, y_L)$ with parameters (4.1a) and of observed $\hat{R}_{\tau\tau}$ from the northern and southern domains (Figure 1, Appendix A).

are largest for small T_F and are always greater than the free-wave speed given by $dy_L/dt_L = 1$. The slope of the line (y_{Lm}, t_{Lm}) is asymptotic to 1, however, as $t_L, y_L \to \pm\infty$.

The contours of $R_{\tau Y}$ exhibit the same asymmetry as found in the observations (Fig. 1) with the absolute maximum value ($\max R_{\tau Y}$) found at negative values of y_L and t_L, (t_{Lam}, y_{Lam}). The magnitude of $\max R_{\tau Y}$ is greatest for $T_F = 1$ and decreases with increasing T_F, accompanied by an increase in $|y_{Lam}|$. Thus, the smaller the friction, the greater the distance $|y_{Lam}|$ of the location of τ that is most highly correlated with Y and the lower the value of $\max R_{\tau Y}$. The fall in $\max R_{\tau Y}$ as T_F increases is related to the increase in $\langle Y^2\rangle_N$. It may be shown from (B1) that, for $T_F^{-1} \to 0$ and fixed α, $\max R_{\tau Y} \sim T_F^{-1/2} 2^{1/2} (\pi/\alpha)^{1/4}$ and $y_{Lam} \sim -\{\alpha^{-1} \times \ln[T_F(\alpha/\pi)^{1/2}]\}^{1/2}$. At zero space lag, $y_L = 0$, $R_{\tau Ym}$ behaves similarly to $\max R_{\tau Y}$ and decreases as T_F increases, while $|t_{Lm}|$ increases. Also, we note that as t_L, $y_L \to -\infty$, the pattern of $R_{\tau Y}$ becomes similar to that of R_{YY}. This results, with $\langle Y_1 Y\rangle$ given by (2.15), because $\langle\tau Y_1\rangle \sim 0$ for $t_L, y_L \to -\infty$.

It is noteworthy that $t_{Lam} = y_{Lam}$ so that the point (t_{Lam}, y_{Lam}) lies on the characteristic line $y_L = t_L$ through $y_L = 0$. From (B1) and (B5), it may be shown that this result holds in general for all cases considered here with $R_{\tau\tau}$ given by (2.7) and with either uniform (2.14) or variable (2.19) τ-variance. Consequently, velocities estimated in these cases using y_{Lam}/t_{Lam} correspond to the free-wave propagation velocities.

Also plotted in Fig. 5 are $\hat{R}_{\xi\xi m}$ and $\hat{R}_{\tau\zeta m}$, along with corresponding (t_{Lm}, y_{Lm}), from the observed northern-domain values in Fig. 1. These are shown for qualitative comparison only as the observed values are obtained from space averages over regions where $\langle\tau^2\rangle$ and $\langle\zeta^2\rangle$ vary strongly with y and that can affect the space-lagged statistics as implied by the results in Section 4b. The qualitative comparison is reasonable, with the closest agreement for R_{YY} obtained with $T_F \approx 3$ days and for $R_{\tau Y}$ with $T_F \approx 6$ days. These values of T_F bracket that of $T_F = 4.25$ days found in

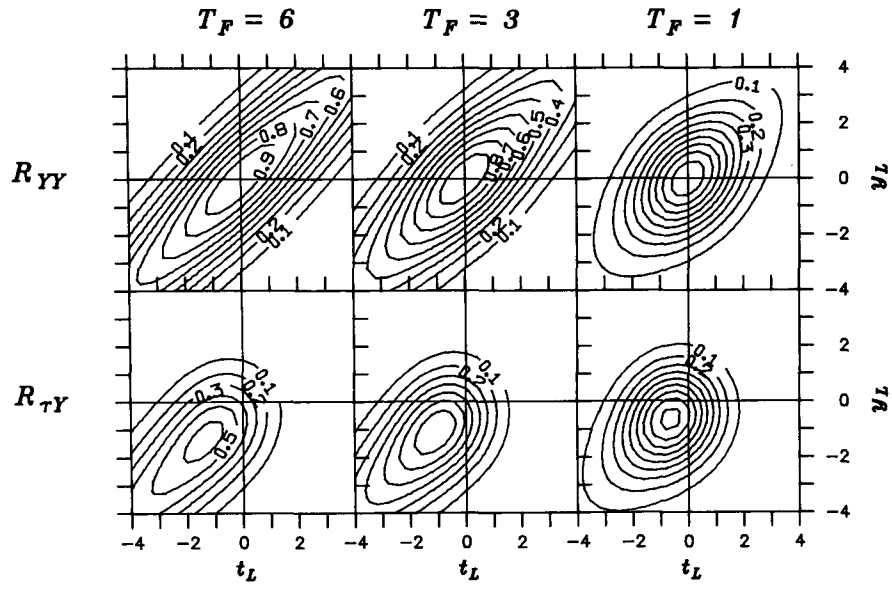

FIG. 4. $R_{YY}(t_L, y_L)$ and $R_{\tau Y}(t_L, y_L)$ for uniform τ-variance (2.14), parameters (4.1), and T_F = 1, 3, 6 days. Contour interval 0.1.

HA by maximizing sea-level variance predicted from (2.3), with constant c and T_F, at four northern-domain sea level stations. Again, we emphasize that y-variability of observed $\langle\tau^2\rangle$ and $\langle\zeta^2\rangle$ prevents quantitative testing of the statistical results from this idealized model.

Differences obtained in R_{YY} and $R_{\tau Y}$ when L and λ are varied are discussed briefly in Appendix D.

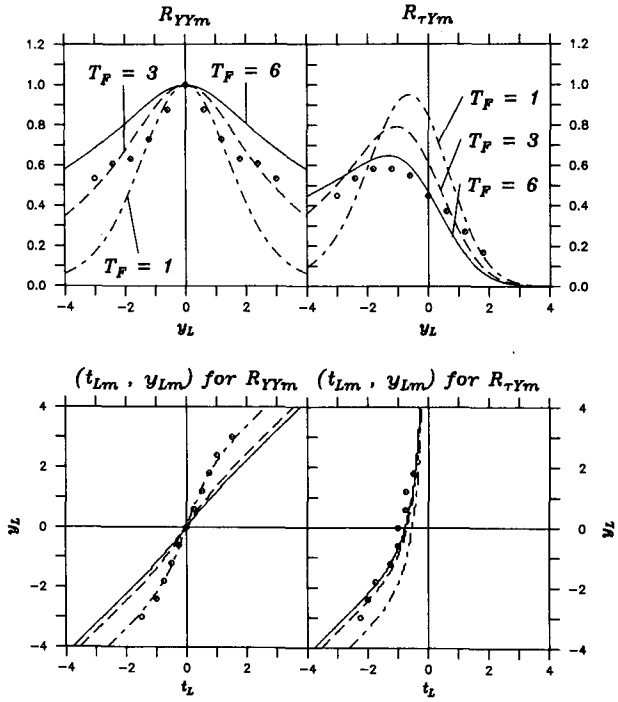

FIG. 5. Maximum values R_{YYm} and $R_{\tau Ym}$ of R_{YY} and $R_{\tau Y}$ for each space lag y_L (top) and the corresponding value of t_L at which the maximum occurs (t_{Lm}, y_{Lm}) (bottom). The absolute maximum values of $R_{\tau Y}$ are max$R_{\tau Y}$ = 0.95, 0.79, 0.65 for T_F = 1, 3 and 6 days, respectively. The small circles are observed values of $\hat{R}_{\zeta\zeta m}$ and $\hat{R}_{\tau\zeta m}$ and corresponding (t_{Lm}, y_{LM}) from the northern domain (Fig. 1, Appendix A).

b. $\langle\tau^2\rangle_y \neq 0$

The case of nonuniform τ-variance (2.19) is investigated with the basic set of parameters (4.1) and with

$$D = 600 \text{ km}. \tag{4.2}$$

The form (2.19) for the y-variability of $\langle\tau^2(y)\rangle$ and the value of D in (4.2) were chosen to model, in an idealized manner, the large increase in τ-variance near Cape Mendocino around 40°N discussed in HA.

A plot of $\langle\tau^2(y)\rangle/\tau_0{}^2$ with this choice of D, and the resulting solution (B7) for $\langle Y^2(y)\rangle/\langle Y^2\rangle_{\max}$ are shown in Fig. 6. It may be seen that $\langle Y^2(y)\rangle_{\max}$ is displaced northward from $\langle\tau^2\rangle_{\max}$. The decay scale of $\langle Y^2(y)\rangle$ for $y \to \infty$ is related to the particular value chosen for T_F in (4.1). In HA, the observed maximum variance in sea level is also found north of the observed $\langle\tau^2\rangle_{\max}$.

Plots of R_{YY} and $R_{\tau Y}$ are shown in Fig. 7 for y = 0, 3 which correspond respectively to positions at and north of $\langle\tau^2\rangle_{\max}$. One of the primary purposes here is to investigate the change in the position y_{Lam} $(=t_{Lam})$ of max$R_{\tau Y}$ as y increases. It may be seen that $|y_{Lam}|$ increases and max$R_{\tau Y}$ decreases as y increases. This is similar to the behavior observed in HA for $R_{\tau\zeta}$ calculated with sea level measured at South Beach, Oregon (44.6°N), just north of the region of large τ-variance along northern California and southern Oregon, and at Neah Bay, Washington (48.4°N), farther north in a region of lower τ variance.

The behavior of R_{YY} in Fig. 7 for t_L, y_L negative,

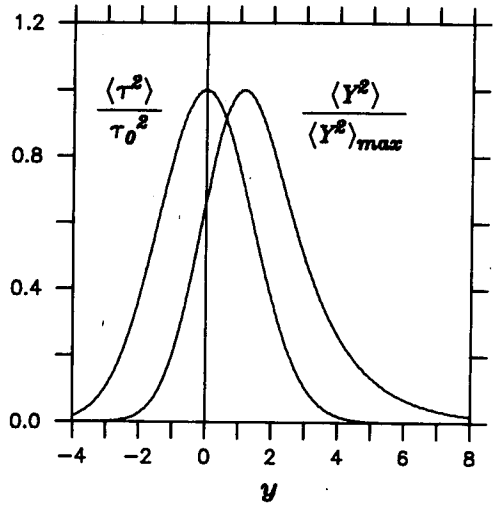

FIG. 6. $\langle \tau^2(y) \rangle / \tau_0^2$ and the resulting solution (B7) for $\langle Y^2(y) \rangle / \langle Y^2 \rangle_{max}$ in the case of nonuniform τ-variance (2.19) with (4.2).

where the spatial correlation scale to the south increases for $y = 3$ compared to $y = 0$, is also similar to the observed behavior for $R_{\zeta\zeta}$ to the south of South Beach and Neah Bay. The increase in correlation scale from south to north for R_{YY} at $y = 0$ is also a feature of the observed $R_{\zeta\zeta}$ calculated for South Beach sea level.

In our example (2.19), $\langle \tau^2(y) \rangle \to 0$ as $y \to \infty$ which results in frictionally damped free-wave propagation to the north asymptotically as $y \to \infty$. For $y = 3$, we find near perfect correlation $R_{YY} \approx 1$ along the characteristic line $y_L = t_L$ for y_L, $t_L > 0$. In addition, the slopes of the other contour lines are asymptotic to the constant value 1 for y_L, $t_L > 0$. This feature is also found for some of the contours of R_{YY} for $y = 0$. That particular behavior is built into the model by the assumed form of (2.19) and is not found in the observations discussed in HA.

5. Results—Frequency domain

We utilize the assumed form of $S_{\tau\tau}$ in (3.5) and calculate the space-lagged squared coherences C_{YY} and $C_{\tau Y}$ as a function of frequency ω and y_L for the same sets of parameters as in Section 4. We also calculate the associated phases Θ_{YY} and $\Theta_{\tau Y}$ and, from Θ_{YY} a dimensionless velocity $c_Y = -\omega y_L / \Theta_{YY}$ characteristic of the Y-fluctuations. Variations in frequency ω are confined to the range $0 \leq \omega' = \omega/2\pi \leq 0.6$ cpd. Note that as part of the full (ω, y_L)-structure of these variables, we obtain theoretical predictions for the variation with ω of quantities that have been extensively calculated from previous observations, namely, the coherence squared and phase between ζ (or v) and local τ, i.e., $C_{\tau Y}$ and $\Theta_{\tau Y}$ at $y_L = 0$, and the propagation velocity c_Y from sea-level (or current measurement) stations separated alongshore by some distance y_{L0}.

It is useful to keep in mind that $C_{\tau\tau}$ has a frequency-independent decay in y_L proportional to $\exp(-2dy_L^2)$. The phase $\Theta_{\tau\tau} = 0$ for $\lambda = 0$ and it corresponds to a constant dimensionless $c_\tau = -\omega y_L / \Theta_{\tau\tau} = \pm 2.2$ for $\lambda = \mp 0.5$.

a. $\langle \tau^2 \rangle_y = 0$

Plots of C_{YY}, Θ_{YY}, c_Y and of $C_{\tau Y}$, $\Theta_{\tau Y}$ for uniform τ-variance (2.14) and for parameters (4.1) with $T_F = 1$, 3, 6 days are shown in Figs. 8 and 9, respectively. As expected with $\langle \tau^2 \rangle_y = 0$, $C_{YY}(y_L) = C_{YY}(-y_L)$, $\Theta_{YY}(y_L) = -\Theta_{YY}(-y_L)$, and $c_Y(y_L) = c_Y(-y_L)$. The coherence scales from C_{YY}, defined approximately as $|y_L|$ for $C_{YY} = 0.5$, are greater for low frequencies. For $\omega' < 0.3$ cpd they are greater for weaker friction, i.e., for larger T_F, and are much larger than the frequency-independent coherence scale of $C_{\tau\tau}$ which is approximately $|y_L| \approx 1$. Isolated points in the (ω, y_L)-plane exist at which the coherence squared is zero, i.e., at which $C_{YY} = 0$. The locations of those points are most easily seen from the accompanying nodes in the phase Θ_{YY}. They strongly influence the (ω, y_L)-patterns of C_{YY}, leading, for example, to very short coherence spatial scales for $\omega' > 0.3$ cpd when $T_F = 6$ days. The points of $C_{YY} = 0$ arise indirectly from zero values of $\{\bar{\tau}\bar{Y}^*\}$ and of $\{\bar{Y}\bar{\tau}^*\}$ for positive and negative y_L, respectively [recall (3.10)].

The zero values of $\{\bar{Y}\bar{\tau}^*\}$ show up directly in $C_{\tau Y}$ (Fig. 9). Mathematically, they are associated with complex zeros of the complementary error function $\mathrm{erfc}(g/d^{1/2})$, where g and d are defined in (C2b,d) and (3.5b). The first complex zero of $\mathrm{erfc}(g/d^{1/2})$, for example, is given approximately by $\mathrm{Re}(g/d^{1/2}) = -1.35$ and $\mathrm{Im}(g/d^{1/2}) = -2.0$ (from Fig. 7.3 of Gautschi, 1964). Using these numbers, we obtain, with (C2b,d) and (3.5b),

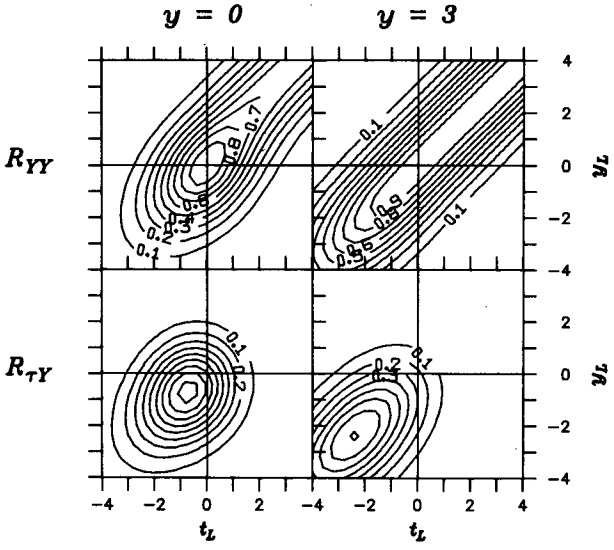

FIG. 7. R_{YY} and $R_{\tau Y}$ for nonuniform τ-variance (2.19), (4.1), and (4.2) at $y = 0$, 3. Max$R_{\tau Y} = 0.95$, 0.81 for $y = 0$, 3, respectively.

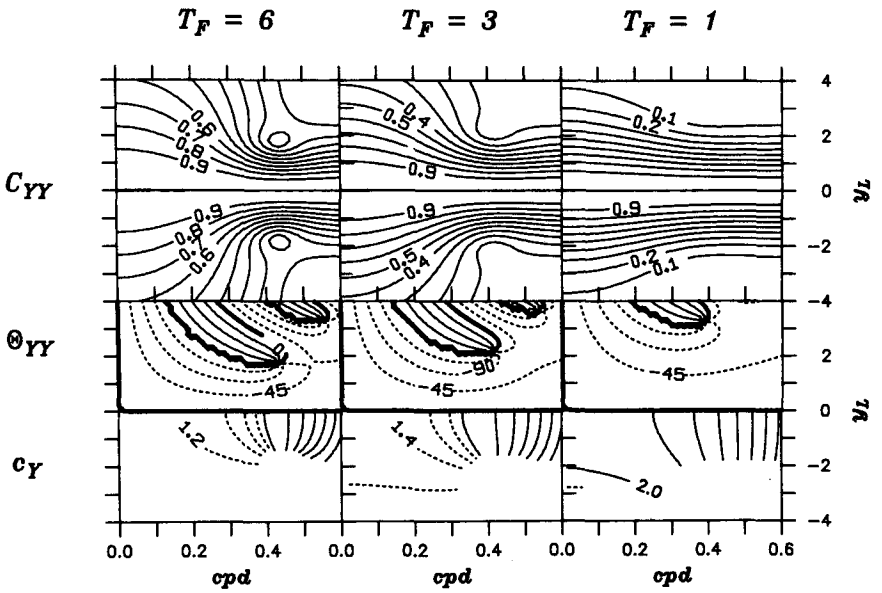

FIG. 8. $C_{YY}(\omega, y_L)$, $\Theta_{YY}(\omega, y_L)$ and $c_Y(\omega, y_L)$ for uniform τ-variance (2.14), parameters (4.1) and T_F = 1, 3 and 6 days. Θ_{YY} is in degrees; $\Theta_{YY}(y_L) = -\Theta(-y_L)$. c_Y is dimensionless (in units of c); $c_Y(y_L) = c_Y(-y_L)$. For C_{YY}, the contour interval is 0.1. For Θ_{YY}, the contour interval is 45°, with $-180° \leq \Theta_{YY} \leq 180°$. The dashed contour lines are for negative phase and the heavy solid lines are 0° or ±180°. For c_Y, the dashed contoured lines run from 1.2 to 1.8 at intervals of 0.2, the solid lines increase from 2 at intervals of 1. Values of c_Y are calculated and contoured only for $C_{YY} \geq 0.2$.

the following values of (ω_0, y_{L0}) for the first zero of $C_{\tau Y}$:

$$\omega_0 \approx 4(c/L)(1 - \lambda^2)^{1/2}(1 + \lambda\chi)^{-1}, \quad (5.1a)$$

$$y_{L0} \approx -(L/c)^2(1 - \lambda^2)^{-1} \times \left[1.35(c/L)(1 - \lambda^2)^{1/2} + \frac{1}{2} T_F^{-1}\right]. \quad (5.1b)$$

It follows for this case that $\omega_0' = \omega_0/2\pi \approx 0.38$ cpd, and that $|y_{L0}|$ decreases with increasing T_F. This agrees with the position of the nodal points of $\Theta_{\tau Y}$ in Fig. 9. We note that the existence of (ω, y_L)-points where $C_{\tau Y} = 0$ does not seem to be associated with the particular form (2.7) assumed for $R_{\tau\tau}$. It may be shown that isolated zero points are present in other cases, e.g., for

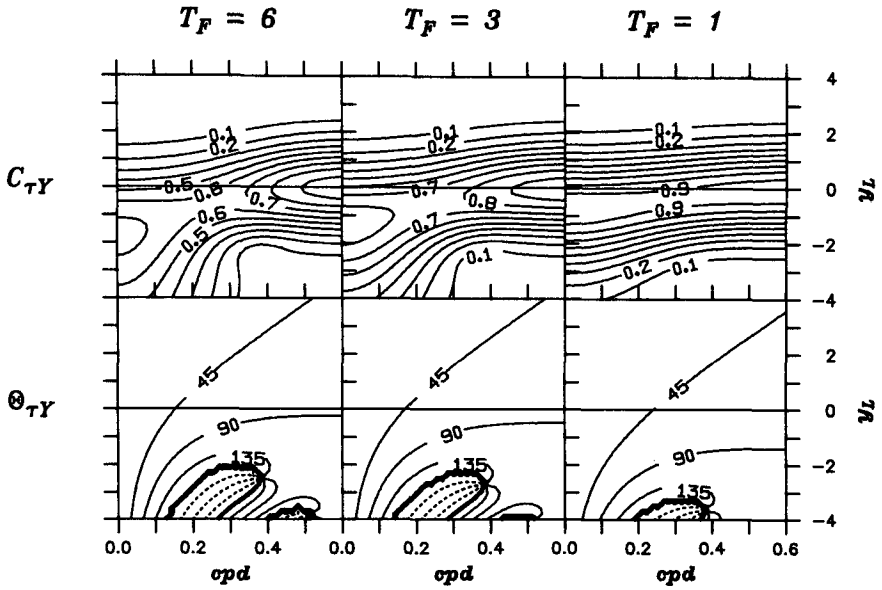

FIG. 9. $C_{\tau Y}(\omega, y_L)$ and $\Theta_{\tau Y}(\omega, y_L)$ for (2.14), (4.1), and T_F = 1, 3 and 6 days. Contours intervals for $C_{\tau Y}$ and $\Theta_{\tau Y}$ are the same as for C_{YY} and Θ_{YY} in Fig. 8.

$R_{\tau\tau}$ with exponential decay dependent on the absolute values of y_L and of t_L. Physically, the $C_{\tau Y} = 0$ points are presumably related to phase randomization by the effect of integrated τ-forcing.

The values of c_Y in Fig. 8 are also, of course, influenced by the zero points of C_{YY}. We see that, for all T_F, $c_Y > c$ with c_Y closest to c for $\omega' < 0.3$ cpd and T_F large.

The plots of $C_{\tau Y}$ for $T_F = 3$ and 6 days (Fig. 9) show that, for low frequencies $\omega' < 0.2$ cpd, the highest values of $C_{\tau Y}$ are found for negative y_L, i.e., for $-2 < y_L < -1$, similar to the values found for y_{Lam} in Section 4. As ω' increases past 0.3 cpd, however, the highest $C_{\tau Y}$ occurs with near-local τ, i.e., with $y_L \approx 0$. From (C1), (C2), and the asymptotic expansion for $\text{erfc}(g_0/d^{1/2})$ (Gautschi, 1964), it can be shown that for $y_L = 0$, $C_{\tau Y}$ $(y_L = 0) \sim 1$ as $g_0/d^{1/2} \to \infty$ with $\arg|g_0/d^{1/2}| < \frac{3}{4}\pi$. Based on the relation $|g_0/d^{1/2}|^2 \gg 1$, we find the following approximate condition on ω for obtaining this asymptotic state:

$$\omega^2 \gg (1 + \lambda\chi)^{-2}[4(c/L)^2(1 - \lambda^2) - T_F^{-2}]. \quad (5.2)$$

For the parameter values in this case, (5.2) gives $\omega' \gg 0.11$, 0.18, 0.19 cpd for $T_F = 1$, 3, 6 days, respectively, in qualitative agreement with the change in patterns of $C_{\tau Y}$ $(y_L = 0)$ as ω increases in Fig. 9. In particular, the weak dependence of this change on T_F, for T_F increasing from 3 to 6 days, is evident in Fig. 9. Condition (5.2) clearly corresponds in (3.2) to the dominance of $(T_F^{-1} - i\omega)\bar{Y}$ over the term $\bar{Y}_y$ involving an alongshore derivative. Consequently, the satisfaction of (5.2) implies a more nearly two-dimensional ($\partial/\partial y \approx 0$) response of $\bar{Y}$ which, corresponding to the loss of importance of alongshore derivatives, might also be described as a condition of local driving. Note that, for $T_F^{-1} \ll 1$, (5.2) is similar to $\omega \gg (1/2)\omega_0$, with ω_0 given by (5.1a). Thus, the condition of local driving at higher ω tends to be associated with the shorter alongshore coherence scales more typical of $C_{\tau\tau}$, which seems to be physically consistent.

In the limit (5.2), we also find

$$\Theta_{\tau Y}(y_L = 0) \sim \tan^{-1}[\omega T_F(1 + \lambda\chi)]. \quad (5.3)$$

Thus, $\Theta_{\tau Y}$ $(y_L = 0) \sim 90$ deg for $\omega T_F(1 + \lambda\chi) \gg 1$. The faster increase toward 90 deg of $\Theta_{\tau Y}$ $(y_L = 0)$ for larger T_F is evident in Fig. 9.

A scaled dimensionless ratio of the resulting spectrum of Y to that of τ, $SR_N(\omega) = SR(\omega)/SR$ ($\omega = 0.13$ cpd) where SR is defined in (C3), is shown in Fig. 10. As is characteristic of all cases studied here, SR_N decreases as ω increases, indicating $\{\bar{Y}\bar{Y}^*\}$ falls off with increasing ω more rapidly than $\{\bar{\tau}\bar{\tau}^*\}$. That falloff steepens as T_F increases. Also shown in Fig. 10 are observed values for SR_N obtained from space-averages of the ζ- and τ-autospectra presented in HA. The overall agreement between observed and these theoretical SR_N is not particularly good, but again the space averages of observed values are over regions where large y-variability in the autospectra of τ and ζ are observed. Nevertheless, in the range 0.1 cpd $\leq \omega' \leq 0.3$ cpd the observed SR_N falls off with increasing ω in a manner qualitatively similar to the theoretical values.

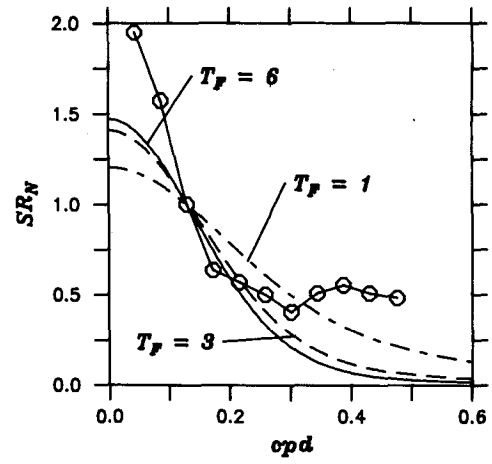

FIG. 10. $SR_N = SR(\omega)/SR$ ($\omega = 1.3$ cpd), where SR is given in (C3), a scaled dimensionless ratio of the spectrum of Y to that of τ with uniform τ variance (2.14) and $T_F = 1$, 3 and 6 days. The circles are corresponding ratios of space-averaged observed autospectra of ζ and τ from Halliwell and Allen (1984) (grid points 2–16).

Theoretical results obtained for C_{YY}, c_Y, and $C_{\tau Y}$ when L and λ are varied are discussed briefly in Appendix D.

b. $\langle\tau^2\rangle_y \neq 0$

The case of nonuniform τ-variance (2.19) is investigated, as in Section 4b, with parameter values (4.1) and (4.2). Results are shown for $y = 0$, 3 in Fig. 11. For $\omega' < 0.4$ cpd, the variations of spatial coherence scales from C_{YY} as a function of y and of y_L are similar to the variation of spatial correlation scales found from R_{YY} in Section 4b. The spatial coherence scale to the south (negative y_L) increases for $y = 3$ compared to $y = 0$. Likewise, at $y = 0$, the coherence scale to the north is much larger than that to the south. The speeds c_Y are generally larger for more negative y and y_L. At $y = 0$, $c_Y > c$ and c_Y decreases for increasing y_L. At $y = 3$, c_Y is close to c, $c < c_Y < 1.2c$, for almost all ω' and y_L, i.e., for $\omega' < 0.5$ cpd and $y_L > -2.5$.

For $\omega' < 0.3$ cpd, the highest $C_{\tau Y}$ are found for negative y_L at a value that decreases greatly from $y_L \approx -0.8$ at $y = 0$ to $y_L \approx -2.5$ at $y = 3$. The magnitudes of $C_{\tau Y}$ at $y = 3$ for $\omega' < 0.3$ cpd are substantially higher for y_L negative, $y_L \approx -2.5$, near the position of $\langle\tau^2\rangle_{\max}$, than for $y_L \approx 0$. This is also consistent with the values found for $R_{\tau Y}$ at $y = 3$ in Section 4b. Also, $\Theta_{\tau Y}$ $(y_L = 0)$ (not shown) behaves differently for each y, increasing more rapidly with ω as y increases. At $y = 3$, $\Theta_{\tau Y}$ $(y_L = 0) > 90$ deg for $\omega' > 0.2$ cpd. This is the only case of those studied here where, for 0

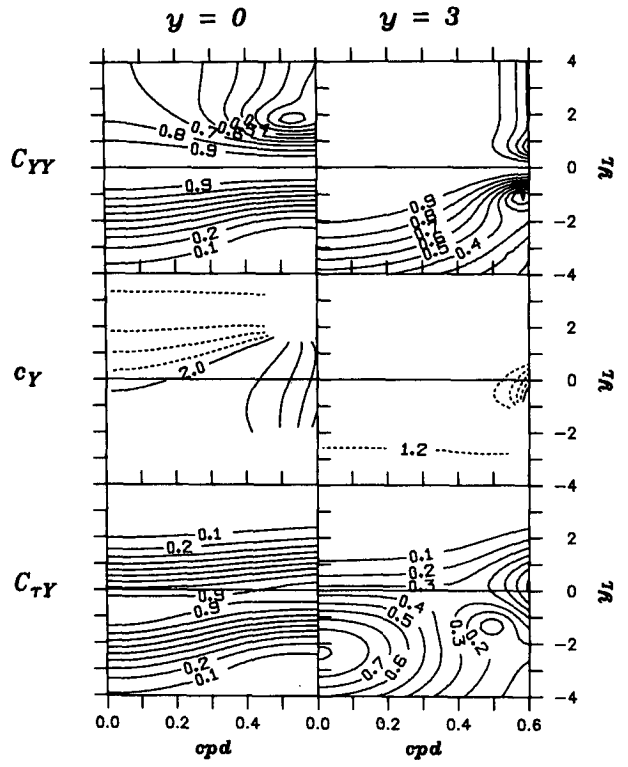

FIG. 11. C_{YY}, c_Y, and $C_{\tau Y}$ for nonuniform τ-variance (2.19), (4.1), and (4.2) at $y = 0$, 3. Contour intervals same as in Fig. 8.

$< \omega' < 0.6$ cpd, $\Theta_{\tau Y}$ ($y_L = 0$) lies outside the range 0 to 90 deg.

6. Summary

The space- and time-lagged cross-correlation coefficients, R_{YY} and $R_{\tau Y}$, calculated from solutions to the forced, first-order wave equation (2.2) using the assumed form (2.7) for $R_{\tau\tau}$ are qualitatively consistent with the $R_{\zeta\zeta}$ and $R_{\tau\zeta}$ correlations found from observations in HA. In particular, the asymmetric pattern in time- and space-lags found for $R_{\tau\zeta}$, in which the largest values of $R_{\tau\zeta}$ occur for negative t_L and y_L, is reproduced in $R_{\tau Y}$.

In the case of uniform τ-variance (2.14), values of the parameters T_F, L and λ are varied individually to gain an understanding of the resultant effects on R_{YY} and $R_{\tau Y}$. It is found that the spatial correlation scales determined from R_{YY} are generally larger than that of τ from $R_{\tau\tau}$, in agreement with observations, and that they increase as T_F and L increase and for λ negative compared with λ positive. Characteristic speeds c_m of Y fluctuations, determined using time lags t_{Lm} for maximum values of R_{YY} at each y_L, are always greater than the free-wave speed c, approaching c more closely for increasing T_F, decreasing L, and for negative λ.

The time and space lags (t_{Lam}, y_{Lam}) at which the absolute maximum value of $R_{\tau Y}(\max R_{\tau Y})$ is found lie on the characteristic line $y_L = t_L$ through $y_L = 0$ and thus determine the correct wave speed, $y_{Lam}/t_{Lam} = 1$. Values of y_{Lam} are negative, with larger absolute values of $|y_{Lam}|$ found for greater T_F and L and for negative λ. Correspondingly, the magnitude of $\max R_{\tau Y}$ is larger for small T_F, large L and negative λ.

For the case of nonuniform τ-variance (2.19), the maximum value of $\langle Y^2(y)\rangle$ is found north of $\langle\tau^2\rangle_{\max}$. Similar behavior occurs in the observed sea-level variance in HA. The R_{YY} and $R_{\tau Y}$ patterns reflect qualitative features found in HA for $R_{\zeta\zeta}$ and $R_{\tau\zeta}$ centered at sea level stations north of the location of an observed large maximum in $\langle\tau^2\rangle$ near Cape Mendocino (40°N). Spatial correlation scales determined from R_{YY} increase to the north of $\langle\tau^2\rangle_{\max}$. In addition, the magnitude of $|y_{Lam}|$ increases for y stations to the north of $\langle\tau^2\rangle_{\max}$, so that $\max R_{\tau Y}$ occurs near the position of the largest τ-variance.

The possibility of using observationally determined values of $R_{\zeta\zeta}$ and $R_{\tau\zeta}$ to extract information on effective magnitudes of T_F is suggested by the change of patterns in Fig. 4. The variations with y of R_{YY} and $R_{\tau Y}$ that result solely from nonuniform τ-variance (Fig. 7), however, indicate difficulties in applying that idea.

The frequency-domain calculations with uniform τ-variance of space-lagged squared coherences C_{YY} and $C_{\tau Y}$ and their associated phases show considerable variations of these quantities with ω and y_L and with the parameters T_F, L and λ. Spatial coherence scales determined from C_{YY} are in general largest at low frequencies ($\omega' < 0.2$ cpd), where the variation with T_F, L, and λ is the same as found for the correlation scales from R_{YY}. Points are found in the (ω, y_L)-plane where $C_{YY} = 0$; these strongly influence the C_{YY} patterns, leading, for example, to shorter coherence scales for $L = 800$ km, compared to $L = 300$ km, when $0.2 < \omega' < 0.5$ cpd. The $C_{YY} = 0$ points are associated with points where $C_{\tau Y} = 0$. The values of (ω_0, y_{L0}) associated with the first zero of $C_{\tau Y}$ are given in (5.1).

The characteristic propagation velocities c_Y, calculated from Θ_{YY}, are typically positive, in the same direction as the free-wave propagation velocity c, and greater than c. Negative values of c_Y are found with $\lambda = +0.5$ (southward propagating τ fluctuations), but only for $\omega' > 0.25$ cpd. In general, values of c_Y are closer to c for low frequencies (e.g., $\omega' < 0.2$ cpd), for larger T_F, smaller L, and for negative λ.

At low frequencies, the largest magnitudes of $C_{\tau Y}$ are typically found at negative values of y_L, similar to y_{Lam} for $\max R_{\tau Y}$. For increasing frequency, however, the location of highest $C_{\tau Y}$ switches to near $y_L \approx 0$. This occurs approximately for frequencies satisfying condition (5.2), which corresponds to a dominance of the time derivative and friction terms in (2.2) over the alongshore derivative term and, thus, to a more nearly two-dimensional ($\partial/\partial y \approx 0$) or locally driven balance. As seems consistent physically, this transition tends to coincide with a reduction in coherence scale of Y (associated with $C_{YY} = 0$ points) to values closer to that

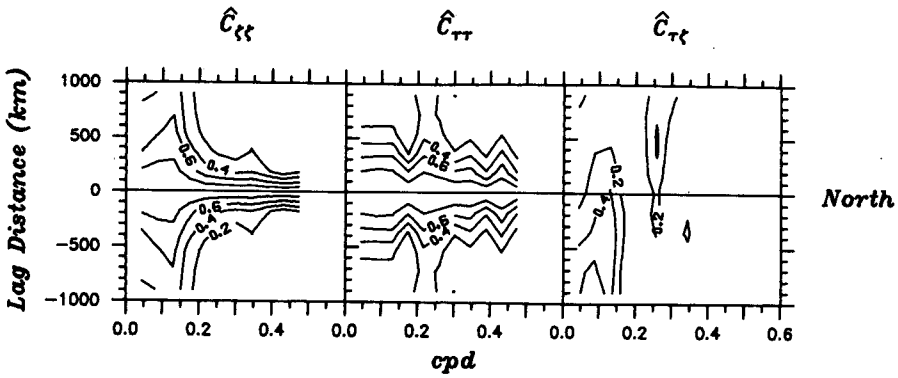

FIG. 12. Observed space-lagged squared coherences calculated from space-averaged cross-spectra with the northern-domain data of Halliwell and Allen (1984). Notation same as for observed correlation coefficients (see Appendix A). The contour interval is 0.2. The unlabeled $\hat{C}_{\tau\zeta}$ contour at $\omega' < 0.15$ cpd, $y'_L < -500$ km is 0.2.

of τ. In agreement with (5.2), the change, as ω increases, of largest $C_{\tau Y}$ from y_L negative to $y_L \approx 0$ occurs at lower frequency for smaller T_F, larger L, and positive λ.

One additional feature of the $C_{\tau Y} = 0$ points should be pointed out. For $T_F = 6$ days in Fig. 9, $C_{\tau Y} = 0$ occurs at $\omega'_0 \approx 0.38$ cpd and at a negative value of y_L close to that for maximum coherence at lower frequency. If cross-spectra between τ at a location near that value of y_L and between ζ at $y_L = 0$ were used to extract the wind-driven component of ζ, a spectrum of the residual series would show a peak near the zero coherence frequency. It might be concluded that around that frequency ζ is not wind-driven and that other processes are responsible for the residual series energy. That, of course, would be incorrect.

Scaled dimensionless ratios of the spectra of Y to the spectrum of τ, show that, in general, the forced Y-spectra fall off more rapidly with increasing ω than the τ-spectrum. The falloff is steeper for large T_F, large L, and positive λ. A similar falloff in the ratio of space-average observed ζ- and τ-spectra from HA is found for 0.1 cpd $< \omega' <$ 0.3 cpd.

To give an indication of how theoretical $C_{\tau Y}$ and C_{YY} compare with observed, in Fig. 12 we show $\hat{C}_{\zeta\zeta}$, $\hat{C}_{\tau\tau}$, and $\hat{C}_{\tau\zeta}$ calculated from space-averaged cross-spectra using the northern-domain data in HA (Appendix A). The coherence scale of $\hat{C}_{\tau\tau}$ is reasonably constant with frequency (200–400 km), increasing somewhat for decreasing ω' and with an indication of larger scales around 0.22 cpd. The coherence scales of $\hat{C}_{\zeta\zeta}$ are $\approx$200 km for $\omega' > 0.2$ cpd, and increase for decreasing ω' to values $\approx$ 800 km for $\omega' \approx 0.13$ cpd. The pattern of $\hat{C}_{\zeta\zeta}$ is, in fact, rather similar to that of theoretical C_{YY} for $T_F = 3$ or 6 days in Fig. 8. For $\hat{C}_{\tau\zeta}$, the highest values are found near $\omega' = 0.13$ cpd for negative space lags in the range 300–700 km. This feature is qualitatively similar to the $C_{\tau Y}$ patterns in Fig. 9 for $T_F = 3$, 6 days, but the increase in $C_{\tau Y}$ ($y_L = 0$) with increasing ω is not evident in $\hat{C}_{\tau\zeta}$. The structure of observed $\hat{C}_{\tau\zeta}$ is presumably related to the fact that the sea-level fluctuations at the northern grid points in the northern domain are forced at southern locations (HA). Thus, $\hat{C}_{\tau\zeta}$ is formed by averages over several points where individual $C_{\tau\zeta}$ are closer in structure to $C_{\tau Y}$ at $y = 3$ (Fig. 11), which is similar to $\hat{C}_{\tau\zeta}$. The same argument does not work well for C_{YY} at $y = 3$, however. Another reason for the differences between the theoretical $C_{\tau Y}$ and the observed $\hat{C}_{\tau\zeta}$ is the idealized form assumed for $S_{\tau\tau}$ in (3.5). Even if the model of the dependence on y_L in (3.5a) is reasonable, d and e/ω vary with frequency. In addition, the spectral shape P (3.6b) of the autospectra of τ is generally a function of y and ω, i.e., $P = P(y, \omega)$. Nevertheless, the theoretical patterns for C_{YY} and $C_{\tau Y}$ produced with this simple model, idealized form of $S_{\tau\tau}$, and limited variation of parameters, show an interesting and surprisingly large range of variability in structure associated with different physical effects and agree qualitatively with observed values on several major features.

Acknowledgments. This research was supported by the Oceanography Section of the National Science Foundation under Grants OCE-8014939 (Coastal Ocean Dynamics Experiment—CODE) and OCE-8026131 ("SuperCODE"). We thank G. R. Halliwell for help in supplying the calculations of observed values for Figs. 1, 10 and 12.

APPENDIX A

Observed Cross-Correlation Coefficients and Cross-Spectra

Space- and time-lagged cross-correlation coefficients from space-averaged covariances for adjusted coastal sea level ζ and the alongshore component of the wind stress τ, $\hat{R}_{\zeta\zeta}[\zeta(y_0)$ versus $\zeta(y)]$, $\hat{R}_{\tau\tau}[\tau(y_0)$ versus $\tau(y)]$, and $\hat{R}_{\tau\zeta}[\zeta(y_0)$ versus $\tau(y)]$, are calculated with the grid-

ded data analyzed by Halliwell and Allen (1984) from along the west coast of North America during June–September, 1973. For that time period, sea level fluctuations are found in HA to have two alongshore domains of variability, one in the north (41.8°N to 52.2°N; grid points 9–16) and an adjacent one to the south (33°N to 41.8°N; grid points 2–9). These domains are characterized by relatively high correlations of ζ within the domains, but poor correlations between them. Consequently, separate sets of correlation coefficients are calculated for each domain.

For $N(=8)$ grid points in each domain, grid interval Δy (=180 km), coordinate $y_i = (i-1)\Delta y (1 \leqslant i \leqslant N)$, and space lag $y_n = n\Delta y (1 - i \leqslant n \leqslant N - i)$, space-lagged correlation coefficients are defined, for example, as

$$R_{\tau\zeta}(y_n, y_i) = \langle \zeta(y_i)\tau(y_i + y_n)\rangle \times [\langle \zeta^2(y_i)\rangle\langle \tau^2(y_i + y_n)\rangle]^{-1/2}, \quad \text{(A1)}$$

where angle brackets denote time average and the time-lag dependence is not shown. The corresponding space-lagged correlation coefficients formed with space-averaged covariances are denoted by a caret and are given, e.g., by

$$\hat{R}_{\tau\zeta}(y_n) = \frac{\sum_{i=I}^{J} \langle \zeta(y_i)\tau(y_i + y_n)\rangle}{[\sum_{i=I}^{J} \langle \zeta^2(y_i)\rangle]^{1/2}[\sum_{i=I}^{J} \langle \tau^2(y_i + y_n)\rangle]^{1/2}}, \quad \text{(A2)}$$

where, for $n \geqslant 0$, $I = 1$, $J = N - n$, and, for $n < 0$, $I = |n| + 1$, $J = N$. The results for each domain are shown in Fig. 1, where the number of space-lags is limited to $|n| \leqslant 5$. Note that when both variables are the same, e.g., ζ, $\hat{R}_{\zeta\zeta}(t, y) = \hat{R}_{\zeta\zeta}(-t, -y)$.

Space-lagged cross-spectral functions, e.g., $\hat{S}_{\tau\zeta}$, formed from space-averaged cross-spectra, are calculated in the same manner as in (A2). Corresponding squared coherences $\hat{C}_{\tau\zeta}$ are then calculated from $\hat{S}_{\tau\zeta}$ as in (3.14).

APPENDIX B

Equations for R_{YY}, $R_{\tau Y}$

a. $\langle \tau^2 \rangle_y = 0$

The evaluation of (2.12), (2.13) and (2.15), with (2.7) and (2.14), gives

$$R_{YY}(y_L, t_L) = \frac{\langle Y_1 Y\rangle}{\langle Y_1^2\rangle^{1/2}\langle Y^2\rangle^{1/2}} = \frac{N_1}{D_1}, \quad \text{(B1a)}$$

$$R_{\tau Y}(y_L, t_L) = \frac{\langle \tau_1 Y\rangle}{\langle \tau_1^2\rangle^{1/2}\langle Y^2\rangle^{1/2}} = \frac{N_2}{D_2}, \quad \text{(B1b)}$$

where

$$N_1 = \tfrac{1}{2}\exp(-\gamma)[\exp(\beta^2/\alpha)\,\mathrm{erfc}(\beta/\alpha^{1/2}) + \exp(\hat{\beta}^2/\alpha)\,\mathrm{erfc}(\hat{\beta}/\alpha^{1/2})], \quad \text{(B1c)}$$

$$N_2 = \left[\tfrac{1}{2} T_F^{-1}(\pi/\alpha)^{1/2}\right]^{1/2} \times \exp(-\gamma)\exp(\beta^2/\alpha)\,\mathrm{erfc}(\beta/\alpha^{1/2}), \quad \text{(B1d)}$$

$$D_1 = \exp(\beta_0^2/\alpha)\,\mathrm{erfc}(\beta_0/\alpha^{1/2}), \quad D_2 = D_1^{1/2}, \quad \text{(B1e,f)}$$

where

$$\mathrm{erfc}(x) = \frac{2}{\sqrt{\pi}}\int_x^\infty \exp(-t^2)dt \quad \text{(B2)}$$

is the complementary error function and

$$\alpha = T^{-2}[\chi^2 + 2\lambda\chi + 1], \quad \text{(B3a)}$$

$$\beta = \tfrac{1}{2}T_F^{-1} + \tilde{\alpha}, \quad \hat{\beta} = \tfrac{1}{2}T_F^{-1} - \tilde{\alpha}, \quad \text{(B3b,c)}$$

$$\tilde{\alpha} = T^{-2}[y_L\chi^2 + \lambda\chi(y_L + t_L) + t_L], \quad \text{(B3d)}$$

$$\gamma = T^{-2}[y^2\chi_L^2 + 2\lambda\chi y_L t_L + t_L^2], \quad \text{(B3e)}$$

$$\beta_0 = \beta(y_L = 0, t_L = 0) = \tfrac{1}{2}T_F^{-1}. \quad \text{(B3f)}$$

Also,

$$\langle Y^2\rangle = \tfrac{1}{2}T_F(cb\tau_0)^2(\pi/\alpha)^{1/2}D_1. \quad \text{(B4)}$$

b. $\langle \tau^2 \rangle_y \neq 0$

The evaluation of (2.12), (2.13), and (2.20), with (2.7) and (2.19), gives

$$R_{YY}(y_L, t_L; y) = N_3/D_3, \quad \text{(B5a)}$$

$$R_{\tau Y}(y_L, t_L; y) = N_4/D_4, \quad \text{(B5b)}$$

where

$$N_3 = \tfrac{1}{2}\exp(-\gamma)\int_0^\infty \exp[-2T_F^{-1}s - (y-s)^2\delta^2 - (y_1 - s)^2\delta^2][\exp(\beta_4^2/\alpha_1)\,\mathrm{erfc}(\beta_4/\alpha_1^{1/2}) + \exp(\hat{\beta}_4^2/\alpha_1)\,\mathrm{erfc}(\hat{\beta}_4/\alpha_1^{1/2})]ds, \quad \text{(B5c)}$$

$$N_4 = \tfrac{1}{2}(\pi/\alpha_1)^{1/4} \times \exp[-\gamma - y^2\delta^2] \times \exp(\beta_3^2/\alpha_1)\,\mathrm{erfc}(\beta_3/\alpha_1^{1/2}), \quad \text{(B5d)}$$

$$D_3 = D_4(y)D_4(y_1), \quad \text{(B5e)}$$

$$D_4(y) = \left\{\int_0^\infty \exp[-2T_F^{-1}s - 2(y-s)^2\delta^2] \times \exp(\beta_2^2/\alpha_1)\,\mathrm{erfc}(\beta_2/\alpha_1^{1/2})ds\right\}^{1/2}, \quad \text{(B5f)}$$

where

$$\alpha_1 = \alpha + \delta^2, \quad \text{(B6a)}$$

$$\beta_2 = \tfrac{1}{2}T_F^{-1} - (y-s)\delta^2, \quad \beta_3 = \beta - y\delta^2, \quad \text{(B6b,c)}$$

$$\beta_4 = \beta - (y - s)\delta^2, \quad \hat{\beta}_4 = \hat{\beta} - (y_1 - s)\delta^2. \quad \text{(B6d,e)}$$

Also,

$$\langle Y^2(y)\rangle = (cb\tau_0)^2(\pi/\alpha_1)^{1/2}D_4^2(y). \quad \text{(B7)}$$

In the calculations of (B5) and (B7), the integrations over s are performed numerically.

APPENDIX C

Equations for S_{YY}, $S_{\tau Y}$

a. $\langle\tau^2\rangle_y = 0$

The evaluation of (3.8), (3.9) and (3.10), with (3.5) and (2.14), gives

$$S_{YY}(y_L, \omega) = \frac{\{\bar{Y}\bar{Y}^*_\dagger\}}{\{\bar{Y}\bar{Y}^*\}^{1/2}\{\bar{Y}_1\bar{Y}^*_\dagger\}^{1/2}} = \frac{N_5}{D_5}, \quad \text{(C1a)}$$

$$S_{\tau Y}(y_L, \omega) = \frac{\{\bar{Y}\bar{\tau}^*_\dagger\}}{\{\bar{Y}\bar{Y}^*\}^{1/2}\{\bar{\tau}_1\bar{\tau}^*_\dagger\}^{1/2}} = \frac{N_6}{D_6}, \quad \text{(C1b)}$$

where

$$N_5 = \exp(-h)[\exp(g^2/d)\ \mathrm{erfc}(g/d^{1/2}) + \exp(\hat{g}^2/d)\ \mathrm{erfc}(\hat{g}/d^{1/2})], \quad \text{(C1c)}$$

$$N_6 = [T_F^{-1}(\pi/d)^{1/2}]^{1/2}\exp(-h)\exp(g^2/d)\ \mathrm{erfc}(g/d^{1/2}), \quad \text{(C1d)}$$

$$D_5 = [\exp(g_0^2/d)\ \mathrm{erfc}(g_0/d^{1/2}) + \exp(\hat{g}_0^2/d)\ \mathrm{erfc}(\hat{g}_0/d^{1/2})], \quad \text{(C1e)}$$

$$D_6 = D_5^{1/2}, \quad \text{(C1f)}$$

and

$$h = dy_L^2 - ey_L, \quad \text{(C2a)}$$

$$g = \tfrac{1}{2}T_F^{-1} + \tilde{g}, \quad \hat{g} = \tfrac{1}{2}T_F^{-1} - \tilde{g}, \quad \text{(C2b,c)}$$

$$\tilde{g} = \tfrac{1}{2}(-i\omega + 2dy_L - e), \quad \text{(C2d)}$$

$$g_0 = g(y_L = 0), \quad \hat{g}_0 = \hat{g}(y_L = 0), \quad \text{(C2e,f)}$$

with, from (3.5b,c),

$$d = (c^2/L^2)(1 - \lambda^2), \quad e = i\omega\lambda\chi. \quad \text{(C2g,h)}$$

Also,

$$SR(\omega) = \frac{\{\bar{Y}\bar{Y}^*\}}{(\frac{1}{2}c^2b^2T_FT)\{\bar{\tau}\bar{\tau}^*\}} = \tfrac{1}{2}(\pi/d)^{1/2}T^{-1}D_5. \quad \text{(C3)}$$

b. $\langle\tau^2\rangle_y \neq 0$

The evaluation of (3.8), (3.9) and (3.13), with (3.5) and (2.19), gives

$$S_{YY}(y_L, \omega; y) = N_7/D_7, \quad S_{\tau Y}(y_L, \omega; y) = N_8/D_8, \quad \text{(C4a,b)}$$

where

$$N_7 = \exp(-h)\int_0^\infty \exp[-2T_F^{-1}s - (y - s)^2\delta^2 - (y_1 - s)^2\delta^2][\exp(g_1^2/d_1)\ \mathrm{erfc}(g_1/d_1^{1/2}) + \exp(\hat{g}_1^2/d_1)\ \mathrm{erfc}(\hat{g}_1/d_1^{1/2})]ds, \quad \text{(C4c)}$$

$$N_8 = \left[\tfrac{1}{2}(\pi/d_1)^{1/2}\right]^{1/2}\exp(-h - y^2\delta^2) \times \exp(g_2^2/d_1)\ \mathrm{erfc}(g_2/d_1^{1/2}), \quad \text{(C4d)}$$

$$D_7 = \tilde{D}_7^{1/2}(y)\tilde{D}_7^{1/2}(y_1), \quad D_8 = \tilde{D}_7^{1/2}(y), \quad \text{(C4e,f)}$$

$$\tilde{D}_7(y) = \int_0^\infty \exp[-2T_F^{-1}s - 2(y - s)^2\delta^2] \times [\exp(g_{10}^2/d_1)\ \mathrm{erfc}(g_{10}/d_1^{1/2}) + \exp(\hat{g}_{10}^2/d_1)\ \mathrm{erfc}(\hat{g}_{10}/d_1^{1/2})]ds, \quad \text{(C4g)}$$

where

$$d_1 = d + \delta^2, \quad \text{(C5a)}$$

$$g_1 = g - (y - s)\delta^2, \quad \hat{g}_1 = \hat{g} - (y_1 - s)\delta^2, \quad \text{(C5b,c)}$$

$$g_{10} = g_1(y_L = 0), \quad \hat{g}_{10} = \hat{g}_1(y_L = 0). \quad \text{(C5d,e)}$$

In the calculations of (C4), the integrations over s are performed numerically.

Also,

$$SR(\omega, y) = \left[\tfrac{1}{2}(\pi/d_1)^{1/2}\tilde{D}_7(y)\right]\left[\tfrac{1}{2}T_FT\exp(-2y^2\delta^2)\right]^{-1}. \quad \text{(C6)}$$

APPENDIX D

Variations of L and λ

Time-domain results obtained when L is varied to L = 300 and 800 km are shown in Fig. 13. The R_{YY}

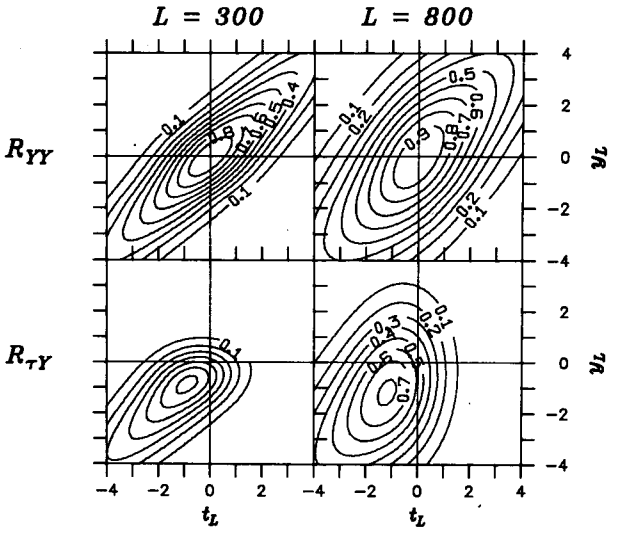

FIG. 13. R_{YY} and $R_{\tau Y}$ for (2.14), (4.1), and L = 300 and 800 km. Contour interval 0.1. Max$R_{\tau Y}$ = 0.73, 0.82 for L = 300 km, 800 km, respectively.

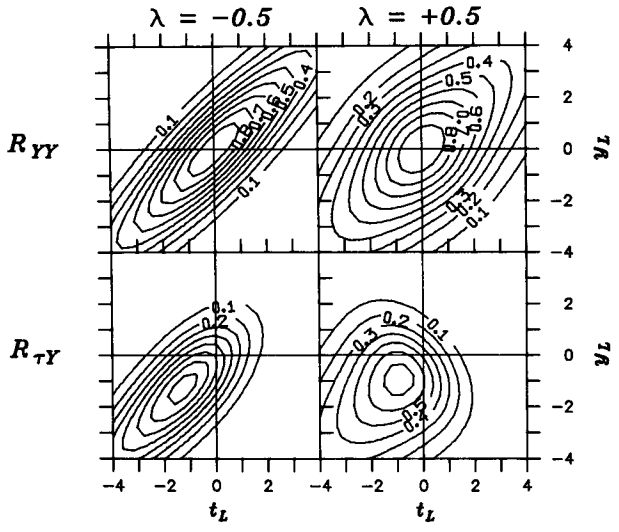

FIG. 14. R_{YY} and $R_{\tau Y}$ for (2.14), (4.1), and $\lambda = \pm 0.5$. Contour interval 0.1. Max$R_{\tau Y}$ = 0.75, 0.85 for $\lambda = +0.5, -0.5$, respectively.

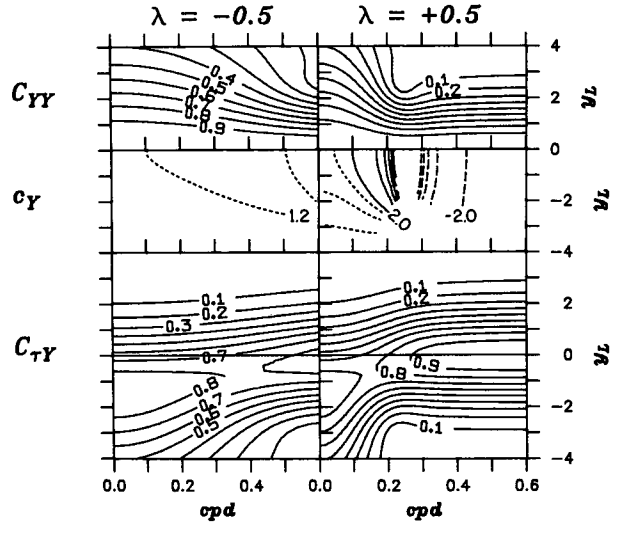

FIG. 16. C_{YY}, c_Y, and $C_{\tau Y}$ for (2.14), (4.1), and $\lambda = \pm 0.5$. Contour intervals same as in Fig. 8, except that long dashed lines in c_Y indicate negative values decreasing from −2 with contour intervals of 1.

spatial correlation scale increases as L increases, as would be expected. Also, a characteristic velocity c_m determined from R_{YY} using (t_{Lm}, y_{Lm}) increases as L increases, reflecting the decrease in magnitude of alongshore gradients and the approach of the motion toward alongshore uniformity. The magnitude of max$R_{\tau Y}$ is greater and occurs at larger $|y_{Lam}|$ for $L = 800$. As L increases, the decay time scale $\alpha^{-1/2}$ for $R_{\tau\tau}$ along the characteristic line $y_L = t_L$ increases. It may be shown from (B1) that, for $\alpha^{-1/2} \to \infty$ and fixed T_F, max$R_{\tau Y} \sim 1$ and $y_{Lam} \sim -T_F$. The increase of max$R_{\tau Y}$ shown in Fig. 13 for increasing L evidently illustrates this tendency toward perfect correlation as the space-time decay scale of $R_{\tau\tau}$ along the characteristic line $y_L = t_L$ goes to infinity. At zero space lag, $y_L = 0$, $R_{\tau Ym}$ and $|t_{Lm}|$ both increase as L increases.

The R_{YY}- and $R_{\tau Y}$-patterns that result when λ is varied to $\lambda = \pm 0.5$, corresponding to $R_{\tau\tau}$ in Figure 2, are shown in Fig. 14. From R_{YY}, the spatial correlation scale is greater with $\lambda = -0.5$, i.e., with τ-fluctuations propagating in the same direction as the free-wave solutions of (2.2) and thus closer to resonant forcing conditions. Also, Y-fluctuation velocities c_m determined using y_{Lm}/t_{Lm} from R_{YY} are again larger than the free-wave velocity c for both values of λ, with those found with $\lambda = -0.5$ being considerably closer to c. The $R_{\tau Y}$-patterns show that max$R_{\tau Y}$ and $|y_{Lam}|$ are greater for $\lambda = -0.5$, consistent with the trend found before with variable L as $\alpha^{-1/2}$ increased. The $\lambda = -0.5$ case of northward propagating τ-fluctuations is the only one of those studied here where $R_{\tau Ym}$ for any y_{Lm} occurs at a time lag that is not negative, i.e., occurs at $t_{Lm} > 0$, which it does for $y_L > 0.8$.

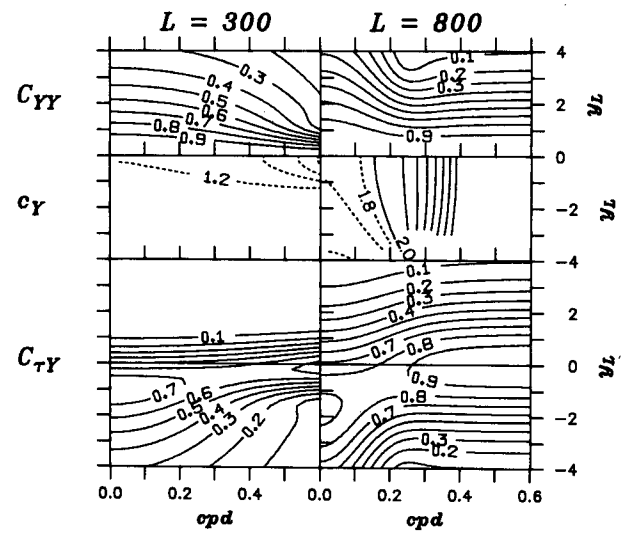

FIG. 15. C_{YY}, c_Y, and $C_{\tau Y}$ for (2.14), (4.1), and L = 300 and 800 km. Contour intervals same as in Fig. 8.

Frequency-domain results obtained for L = 300 and 800 km are shown in Fig. 15. The spatial coherence scale from C_{YY} is substantially larger for $\omega' < 0.2$ cpd with L = 800 km. The coherence scale decreases as ω' increases past 0.2 cpd for L = 800 and past 0.5 cpd for L = 300. These patterns are related to the $C_{YY} = 0$ points and correspond to the fact that the frequency ω_0 in (5.1a) for $C_{\tau Y} = 0$ decreases as L increases, while $|y_{L0}|$ increases. The values of c_Y are greater than c, with those for L = 800 km substantially larger than those for L = 300 km. This is similar to the variation in c_m found above.

For low frequencies, the largest $C_{\tau Y}$ are found for L = 800 km at greater negative y_L and with higher values than for L = 300 km. Both of these results are similar to those found for max$R_{\tau Y}$. At the same time, for L = 800 km the transition, as frequency increases,

to locally driven flow, with highest $C_{\tau Y}$ found near $y_L = 0$, occurs at $\omega' = 0.2$ cpd. This is a much lower transition frequency than that inferred from Fig. 15 for $L = 300$ km, and is in agreement with (5.2). In addition, as ω increases, $\Theta_{\tau Y}$ ($y_L = 0$) (not shown) increases toward 90 deg much more rapidly with $L = 800$ km. Plots of $SR(\omega)$ (not shown) show a substantially steeper falloff for increasing ω with larger L.

Results obtained with $\lambda = \pm 0.5$ are shown in Fig. 16. The coherence scale from C_{YY} is larger at almost all frequencies for $\lambda = -0.5$. For $\lambda = +0.5$, a $C_{\tau Y} = 0$ point occurs at $\omega'_0 = 0.23$ cpd and $y_{L0} = -3.2$ and this is strongly reflected in the overall C_{YY}- and Θ_{YY}-patterns. In fact, for $\lambda = +0.5$ the values of c_Y obtained for $\omega' > 0.25$ cpd are negative, so that Y-fluctuations appear to propagate in the same southward direction as the τ-fluctuations. When $\omega' < 0.25$ cpd, however, c_Y is positive and larger than c. With $\lambda = -0.5$, c_Y is always positive and is much closer to c, i.e., $c < c_Y < 1.4c$, for all ω and y_L.

In the $C_{\tau Y}$-plots, the highest values for $\lambda = -0.5$ are found for negative y_L, i.e., $y_L < -1$, over a wide range of frequencies, $0 \leq \omega' \leq 0.3$ cpd. On the other hand, for $\lambda = +0.5$, the change, as ω' increases, to locally driven flow, with highest $C_{\tau Y}$ found for $y_L \approx 0$, occurs at low frequency near $\omega' \approx 0.15$ cpd. In both instances, this behavior is consistent with (5.2). The phase $\Theta_{\tau Y}(y_L = 0)$, is much smaller for all ω when $\lambda = -0.5$. For $\lambda = +0.5$, $\Theta_{\tau Y}(y_L = 0) \approx 90$ deg for $\omega' > 0.3$ cpd. $SR(\omega)$ shows a steeper falloff for increasing ω with $\lambda = +0.5$.

REFERENCES

Allen, J. S., 1984: A simple model for stratified shelf flow fields with bottom friction. *J. Phys. Oceanogr.*, **14,** (in press).

——, and R. L. Smith, 1981: On the dynamics of wind-driven shelf currents. *Phil. Trans. Roy. Soc. London,* **A302,** 617–634.

Brink, K. H., 1982: The effect of bottom friction on low-frequency coastal trapped waves. *J. Phys. Oceanogr.*, **12,** 127–133.

——, and J. S. Allen, 1978: On the effect of bottom friction on barotropic motion over the continental shelf. *J. Phys. Oceanogr.*, **8,** 919–922.

——, and J. S. Allen, 1983: Reply. *J. Phys. Oceanogr.*, **13,** 149–150.

Clarke, A. J., 1977: Observational and numerical evidence for wind-forced coastal trapped long waves. *J. Phys. Oceanogr.*, **7,** 231–247.

Gautschi, W., 1964: Error function and Fresnel integrals. *Handbook of Mathematical Functions,* M. Abramowitz and I. A. Stegun, Eds., Natl. Bur. Stand., Appl. Math. Ser., No. 55, 295–329.

Gill, A. E., and A. J. Clarke, 1974. Wind-induced upwelling, coastal currents and sea-level changes. *Deep-Sea Res.*, **21,** 325–345.

——, and E. H. Schumann, 1974: The generation of long shelf waves by the wind. *J. Phys. Oceanogr.*, **4,** 83–90.

Halliwell, G. R., Jr., and J. S. Allen, 1984: Large scale sea level response to atmospheric forcing along the west coast of North America, summer 1973. *J. Phys. Oceanogr.*, **14,** 864–886.

Hamon, B. V., 1976: Generation of shelf waves on the east Australian coast by wind stress. *Mém. Soc. R. Sci. Liège,* **10,** 359–367.

Huyer, A., R. L. Smith and E. J. C. Sobey, 1978: Seasonal differences in low-frequency current fluctuations over the Oregon continental shelf. *J. Geophys. Res.*, **83,** 5077–5089.

Kundu, P. K., and J. S. Allen, 1976: Some three-dimensional characteristics of low frequency current fluctuations near the Oregon coast. *J. Phys. Oceanogr.*, **6,** 181–199.

Smith, R. L., 1974: A description of current, wind, and sea level variations during coastal upwelling off the Oregon coast, July–August 1972. *J. Geophys. Res.*, **79,** 435–443.